Powder Technology 318 (2017) 471–483

Contents lists available at ScienceDirect

Powder Technology

journal homepage: www.elsevier.com/locate/powtec

X-ray tomography investigations of mono-sized sphere packing structures in cylindrical containers

Joerg Reimann *, Jerome Vicente, Emmanuel Brun, Claudio Ferrero, Yixiang Gan, Alexander Rack

Karlsruhe Institute of Technology, P.O. Box 3640, 76021 Karlsruhe, Germany

ARTICLE INFO

Article history:
Received 8 February 2017
Received in revised form 9 May 2017
Accepted 14 May 2017
Available online 25 May 2017

Keywords:
Granular materials
Packing structure
Packing density
Vibration
Sphere packing

ABSTRACT

The structure of mono-sized sphere packings (diameter d) in cylindrical containers (diameter D and height H) both with and without inner cylinders (diameter D_i) has been investigated in detail by means of advanced X-ray computed tomography. The geometrical parameters were varied in a wide range; in all experiments 1d vertical vibration was applied. Five experiments were selected with characteristically differing local packing structures. The influence of container geometry, filling and vibration procedures on the formation of regular packings is discussed and a simple correlation is presented to assess whether structured packings occupy a significant fraction of the total packed volume.

For a packing with moderate densification, the regular structures are restricted to small wall zones and a random packing exists in the largest part of the packing volume. By selecting appropriate vibration parameters, the zones with regular structures can increase considerably and can persist in the total packed volume. The increasing crystallisation causes an increase of the container packing fraction. For cylinders with $H/D \gg 1$ and moderate D/d, regular structures develop preferentially in radial direction from a hexagonal layer at the concave wall. For $H/D < 1$ and $D/d \gg 1$, hexagonal dense structures grow preferentially above the flat bottom plate and can occupy a great portion of the total volume. The role of granular convection on these crystallisation processes has been addressed. Previous statements that the thickness of wall zones is $\approx(4–5)d$ are not generally valid for mono-sized sphere packings; the development of a comprehensive correlation is the task of a future work.

Structural details of the packings close to concave, plane and convex walls are analysed via void fraction distributions, sphere centre positions, contact angle distributions, coordination numbers, radial distribution function and Voronoi tessellation. The combination of these methods provides a comprehensive understanding of structural details. Only a few characteristic results are presented; special topics will be the subject of forthcoming publications.

1. Introduction

The knowledge of the packing structure of granular beds is of importance for a range of technical applications [1–4] where heat and mass transfer processes depend on the non-homogeneous porosity in the packed beds. Historically, first detailed investigations with spherical particles aimed to determine the main global structural property, i.e. the packing fraction γ_t in the container defined as the ratio of the volume occupied by the particles to the total packing volume (the corresponding void fraction ε_t is then $\varepsilon_t = 1 - \gamma_t$). Systems with one nominal sphere diameter d (single-sized spheres) were investigated as well as mixtures of spheres with two or more diameters (binary, ternary systems) [5–18].

Besides technical applications, the packing of mono-sized spheres received significant interest for the simulation of crystallisation processes [19–27]. In this work, the term crystallisation is used for the generation of regular packings. Various measures were devised to quantify packing arrangements mostly analysing structures far away from walls. In the present investigation, some of these measures are used for the first time in detail to quantify packing structures induced by walls.

An extensive host of literature exists about packing topics, thus the present work is not aimed to provide a comprehensive overview and only a few pertinent papers are actually revisited and critically discussed in the light of our findings.

In technical applications, large amounts of spheres are often required and produced economically by processes which generally result in sphere diameters with appreciable variations in respect to the nominal diameter d, sphericity, roughness etc. Information on diameter tolerances was sometimes given by listing the used mesh [8] sizes without information on diameter distributions. Furthermore, non-spherical pebbles can exist within a mesh class, which may have been sorted out or not [8,11]. The reason of these comments is that packing structures depend sensitively on the above-mentioned quantities and some results from previous investigations might have been masked by

* Corresponding author.
E-mail address: joerg.reimann@partner.kit.edu (J. Reimann).

http://dx.doi.org/10.1016/j.powtec.2017.05.033
0032-5910/

inaccurate specifications. In the following, we use the term "mono-sized" for spheres with negligible tolerances regarding diameter and sphericity. The present experiments have been performed using spheres with deviations from nominal diameter and sphericity of 1% or less. Systematic tomography investigations on the influence of larger deviations on packing structures are currently performed.

It has been known for a long time that within a packed bed the packing structure is not homogeneous: in the bulk, a random particle packing can exist, whereas a structured packing occurs in zones near the walls, as demonstrated first by measured void fraction fluctuations [13–17].

The influence of these regular structures on γ_t could not be investigated in detail for many years and experiments focussed on the measurement of γ_t as a function of the container dimensions (for cylindrical containers: diameter D, height H). The results were presented as a function of d/D, see Fig. 1, and d/H, see e.g. [6,8,11,18]. Characteristically, γ_t decreases with increasing d/D and d/H due to the increase of the volume fraction of the wall layers, where, in the part adjacent to the wall, the local packing fraction is the smallest, as outlined in Section 4.3.

One of the key quantities is the extrapolated value for γ_t at $d/D = 0$ and $d/H = 0$, representative of random close packing (RCP) in infinitely large containers. The value γ_{RCP} is also important for crystallisation processes. Recent X-ray tomography experiments [25] confirmed the value $\gamma_{RCP} \approx 0.64$, already determined in the mid-20th century [8,10,13].

Fig. 1 shows also results for random loose packing [6]: the extrapolated packing fraction for $d/D = 0$ is close to 0.59 [25].

However, there has been also evidence that structured packings must not be restricted to small wall zones but can exist in the largest part of the packed volume: Using cylinders with $H/D < 1$, $D/d > 20$ and $H/d \approx 15$, hexagonal close packed structures were observed [12,21] which had built up on the bottom plate. Values for γ_t were not given, however, owing to the dominance of hexagonal structures it is expected that γ_t was significantly greater than γ_{RCP}. For long cylinders with $D/d \approx 10$ [22] the ordered structures had built up on the cylinder wall and $\gamma_t > 0.65$ was measured. More recently, detailed experiments with different modes of vibration and filling procedures were performed by An et al. [28–30] using cylinders with moderate H/D values. For 2d and 3d vibrations, very high packing fractions were obtained (Fig. 1) and hexagonal structures at the packing surface were observed.

In the above cited investigations, the cavity was filled with all spheres before starting to vibrate (one step filling, 1sf). By continuous filling (small feeding rates during vibration) or batch-wise filling (stepwise filling with subsequent vibration) [20,28–30], even higher packing fractions were achieved, Fig. 1, because this procedure favours the most the generation of dense structures.

To summarise, it can be stated that packing fractions γ_t above the random close-packing curve in Fig. 1 result from the contribution of regular packing zones. This implies that the curve for maximum packing fractions in very large containers should reach $\gamma_t \approx 0.74$, the maximum value corresponding to hexagonal dense packings, and must decrease with increasing d/D and d/H. Already MacRae [7] stated "…there are only two explicitly definable states of a packed bed: (a) where the porosity is a maximum, and any increase would give rise to a cloud of separated particles…(b) where the bed is completely ordered and a close-packed arrangement exists. Any condition intermediate between these two is not defined, in a sense that mechanical energy imparted to the bed might change the voidage."

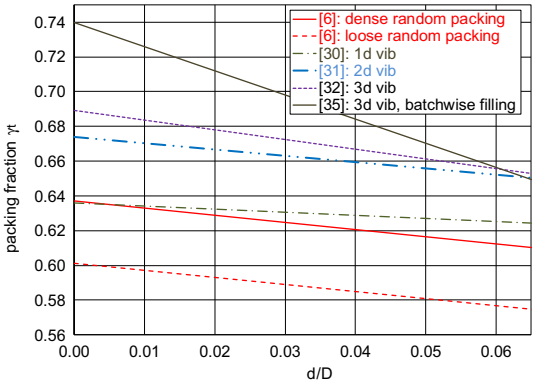

Fig. 1. Correlations for container packing fractions γ_t of spheres of diameter d in cylinders of diameter D and height H.

As mentioned above, investigations of internal packing structures began with the measurement of radial void distributions in cylindrical containers [13–17,31–33], cf. also Fig. 2. Starting at the wall, fluctuations were observed which damp out after distances of (4–5)d. The measured minimum void fractions of the wall layers were >0.2 and the bulk packing fraction was $\gamma_b \le \gamma_{RCP}$. Results for a flat wall [14] did not differ significantly. These early results were the basis for many empirical correlations, cf. the overview [34]. It should be noted that these experiments were affected by rather limited spatial resolutions and accuracies.

The use of X-ray computed tomography, CT, has expanded extraordinarily the experimental potential for studying packing structures: beside measuring much more accurately radial and axial void distributions (RVD and AVD, respectively), advanced CT facilities enable the determination of topological quantities such as contact numbers, contact angle distributions, and even contact surfaces [24,25,35–48].

In parallel to this experimental progress, the mathematical description of the interaction and kinetics of large numbers of spheres (discrete element modelling, DEM, techniques), originally developed by Cundall [49], has also advanced significantly and has become a powerful tool not only for packing experiments but also for mechanical particle-to-particle interactions and granular flows, see e.g. [50–51].

Fig. 2 shows a comparison between CT results and DEM simulations [52] for mono-sized spheres in a cylindrical container with $\gamma_t = 0.616$. Regular structures are observed both at the cylinder wall and the bottom and top plates; a bulk zone with random packing exists in between. Fig. 2(a) and (c) shows the CT positions of the sphere centres in the horizontal x′-y′ plane and in the plane defined with the radius r′ and the vertical direction z′, respectively. Fig. 2(b) and (d) displays CT and DEM void fraction distributions, respectively. The void distributions are well matching, along with the characteristic sphere centre positions close to walls, see the DEM results in [52].

The benefits of combining CT with DEM were outlined in [53], where the CT measurement errors can be overcome by introducing small displacement perturbations to reach the equilibrium state using DEM.

2. Influence of container geometry, filling and densification techniques on packing structures

In most technical applications, the aim is to generate dense particle beds in containers, associated with the occurrence of regular packing structures. The complex interaction of geometrical parameters, particle material properties, filling as well as vibration modes on the formation of regular structures makes it difficult to draw general conclusions.

2.1. Container geometry

Most packing fraction experiments were performed with vertical cylinders as containers; relevant parameters are D/d, H/d and H/D. For annular containers (inner diameter D_i), additional parameters come into play, namely D_i/d and the dimensionless annular width $(D - D_i)/d$. For rectangular containers, corresponding ratios can be defined embracing the lateral dimensions of their basis.

The particle packing in the containers can have a free upper particle surface, the containers can have a movable piston on the top as well as a lid which is tightened during vibration. Alternatively, the containers can be closed, except for a small opening for filling purposes. The packing

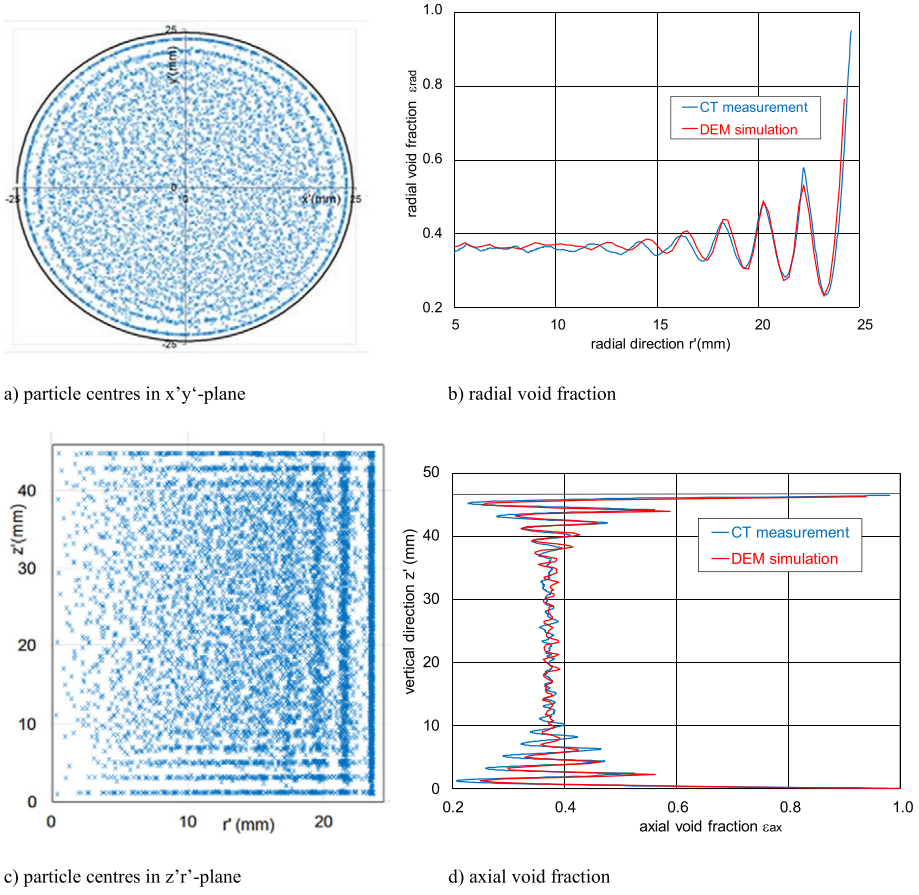

a) particle centres in x'y'-plane

b) radial void fraction

c) particle centres in z'r'-plane

d) axial void fraction

Fig. 2. Sphere centre positions and void fraction distributions: comparison between CT measurements and DEM simulations [52].

condition at the top of the packing influences the development of regular structures and by this γ_t. In previous works, details of the conditions on the packing top were often not given.

Cylindrical containers with H/D ≫ 1 were used in order to minimise top and bottom effects [6–11,18,19,22]. Circular containers with H/D ≈ 1 are of interest, compare Fig. 2, if the system is subjected afterwards to uniaxial compression tests, UCTs, used for the determination of mechanical properties of particle beds [54]. In these cases, a movable disk/piston at the top is generally used in order to generate a horizontal packing interface. For some applications, values of H/D ≪ 1 are of interest [54]. In this case, the curvature effect D/d disappears and the geometry approaches that of a shallow bed. There are only a few experimental investigations on packing structures in annular geometries. For an annular width of 7d [14], the radial void fluctuations were interconnected, whereas for 14d [55] a bulk zone existed in between. Total packing fractions were <0.62. In an experiment with an annulus width of 11d and D/d = 120 [27] an almost perfect hexagonal dense wall structure along with a very large packing fraction ($\gamma_t \approx 0.69$) was obtained. However, for D/d = 120, curvature effects are small and the overall structure is close to that of a prismatic container without lateral constraints.

Prismatic containers are characteristic for e.g. closed blanket components in future thermonuclear fusion reactors [4]. In such containers, the dimension w′ is characteristically <10% of the two other dimensions (*shallow containers*) and w′/d is in the range of 20. These components must be filled through small pipes positioned at the highest point of the system [56].

The regularity of packing structures close to plane walls can be much more pronounced than close to curved walls, as shown in detail further down. For shallow containers, regular wall structures at opposite walls might easily become interconnected.

2.2. Filling procedure

As mentioned above, 1sf, followed by vibration is the standard technique. Continuous or batch-wise filling [20,28–30] requires a proper control of the vibration processes, which might be difficult to achieve in technical applications. According to [4], the prismatic containers were connected to a continuous feeding line [56] and particles were filled in as long as possible during vibration. In smaller experiments, a step-wise procedure was used [57].

2.3. Vibration modes

In order to generate reproducible results, present vibration devices operate in a sinusoidal mode, either 1d vertically, 2d horizontally, or 3d. Vibration is characterised by i) the vibration intensity $\Gamma = a(2\pi f)^2 / g$, where a, f and g are the amplitude of the pulsation, the vibration frequency and the gravitational acceleration, respectively, and ii) the normalised vibration amplitude a/d.

Vibration can be applied by using individual pulses, separated by intervals where the system comes to rest [19,22] or by continuous vibration, which is the standard procedure. In most experiments, the total container is vibrated. For the sake of comparison with DEM simulations, the vibration was restricted to the bottom plate [21].

For a confined packing at the top using a piston with a constant load on the top, the packing fraction decreases with increasing load [58]. This method differs from that also used in the present experiments, where the top lid can be tightened in such a way that individual particles can still move but granular convection is suppressed.

For a given experimental set-up the packing fraction first increases with Γ, keeping a/d constant, until a maximum value is reached, designated as Γ_c (*irreversible compaction branch* according to [22]), and then

decreases. The same tendency is also observed for the variation of a/d at constant Γ. However, a further significant densification was obtained by decreasing Γ (*reversible process*) when Γ_c was reached [22].

Even if only vertical 1d vibration with a free particle bed surface is considered, the optimum vibration parameters depend in a very complex way on the packing parameters. One reason for this is the influence of granular convection on crystallisation. Characteristically, axisymmetric convection rolls can occur in cylindrical containers with an upward flow in the centre and a downward flow at the cylinder wall [59]. In rather unconfined systems (large ratios of lateral dimension to d), granular convection was observed for Γ not significantly larger than unity [60]. However, with decreasing D/d this value increases significantly; e.g. no convection occurred at D/d ≈ 10, H/d ≈ 500 and Γ ≈ 3 [22] where a radially dominated crystallised structure was observed. For D/d ≈ 35, H/d ≈ 16 and Γ ≈ 6, an initial convection roll came to rest, apparently promoting the crystallisation which started at the bottom [21]. The decrease of convection activity with time was also measured by [61] who reported the presence of four flow regimes when increasing Γ: a) slowly stabilising crystallisation, b) convection, c) fast stabilising crystallisation, d) unstable crystallisation. Surprisingly, the existence of the convection regime between two crystallisation regimes was detected.

At present, there is no known relationship between vibration parameters promoting crystallisation and packing parameters. For correlating the strength of axisymmetric convection rolls, the parameter $(DH)^{0,5}/d$ was introduced [62]. However, the authors stated that their correlation is not suitable for defining a limit where convection boosts crystallisation.

The subject of the present work is the inception of crystallisation induced by walls. It should be noted that the presence of walls is not mandatory for crystallisation of packings, as demonstrated both experimentally [30] and by DEM simulations [59,63].

3. Experiments

3.1. Experimental parameters

Continuing previous CT experiments on the morphology and topology of mono-sized sphere packings in cylindrical containers [36,37,39,41,43,45,47], a measurement campaign started in 2013 with the aim of broadening the existing parameter range D/d, H/d, and, by using internal cylinders of diameter D_i, the parameters Di/d and the dimensionless annular gap width $(D - D_i)/2/d$, see Fig. 3(a). All container parts consisted of Plexiglas.

Mono-sized aluminium spheres with d = 2.34, 3.2, 4.0 and 5.0 mm were used. Optical micrographs of the spheres (2D projections) were examined with the Leica QWin Suite (version 3.1.0) in order to measure sphere size distributions as well as the sphere roundnesses. Diameter tolerances were at maximum 1%, as well as deviations from the roundness index $R_{index} = 1$.The diameters of the cylindrical containers were D = 30, 50, 80 mm and the internal cylinder diameters were D_i = 0.6, 2.0, 3.0, 5.0, 10.0, 20.0, and 30.0 mm. The packing height was 25 < H < 90 mm. Using these dimensions, D/d varies between 6 and 34 and H/d is at maximum ≈38 for 2.3 mm spheres and ≈18 for 5 mm spheres.

At present, more than thirty CT experiments have been performed and the maximum number of particles in a single experiment was >100,000. First results were presented in [47].

The containers were filled by gently pouring down the spheres to form the initial packing. A 10 mm thick Plexiglas disk was placed at the top and the initial packing fraction was determined by height measurements at different positions. The weight of this disk corresponds to the weight of less than one particle layer of 2.3 mm spheres and, therefore, does not result in a significant particle bed compaction. The containers were fixed on the table of the vibrating apparatus (Renfert Vibrax REF 1830000) and were vibrated 1d vertically with f = 50 Hz

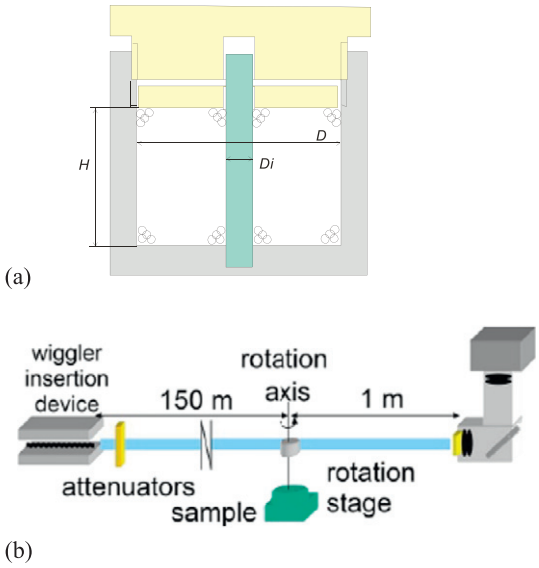

Fig. 3. Schematics of (a) container, (b) tomography experimental set-up [64].

or 100 Hz. For each frequency, four power steps could be selected. Vibration parameters were measured by an accelerometer (Bruel & Kjaer Type 425), fixed at the container top. The measured ranges were 0.5 < Γ < 6 and 0.04 mm < a < 0.3 mm. With this, the vibration parameters are similar to those in [21,28].

The packings were vibrated with constant vibration parameters either with the Plexiglas disk at the top or with a free particle bed surface. The comparison of results with/without disks showed that the disk has a negligible influence on the densification process. The containers were vibrated until no further densification changes occurred, controlled by packing fraction measurements at different time steps. Vibration periods were up to 1 h. At the end of this vibration period, the top lid was screwed downwards in steps using larger vibration parameters in order to achieve a plane horizontal packing boundary which improved to a certain degree the sphere coverage at the top. During this procedure, the dilatancy of the vibrated packing was controlled in such a way that particles could still change their positions but granular convection was suppressed. This procedure influences γ_t only remarkably when granular convection existed, see Section 4.2. In this case, besides improving the top wall coverage, the top packing structure becomes similar to that of the bottom zone. When the first vibration period resulted in a rather stiff packing, the subsequent vibration procedure had an immaterial influence on packing structures.

Beside the preparation of the tomography experiments, many packing fraction experiments were performed, not discussed in this article. The sphere structures at all Plexiglas walls were documented by photographs and videos at different steps during the vibration period.

3.2. Microtomography and data analyses

The CT data of the specimens were acquired at the ESRF, Fig. 3(b) [64]. Two experimental campaigns were performed, one on the ID17 beamline and concerns samples A, B and C; the samples D and E were imaged at the ID19 beamline.

The X-ray beam energy for the ID17 measurements was 140 keV (monochromatised by a double silicon (1 1 1) Laue crystal system). The sample-to-detector distance was approximately 11 m. The imaging detector was a Fast Readout LowNoise (FReLoN) 2k CCD camera and the related optical equipment features a 90 mm × 90 mm field of view with an effective pixel size of 48 μm × 48 μm. Due to the aspect ratio of the beam (5 mm height vs. 9 cm width) the samples were vertically moved after each scan. Each sub-volume was scanned with 2000 angular positions for the total range of 360°.

On ID19, in order to reach a sufficient photon flux density as well as a homogeneous wave front for high quality imaging, the beamline was operated in pink beam mode. The resulting broad spectrum is polychromatic but narrow enough for microtomographic applications. The effective spectrum was trimmed via the gap of the wiggler insertion device and suitable filters were inserted (e.g. a mean photon energy of 70 keV was used [65] for Exps. D and E, see Section 4.1. The sample-to-detector distance was approximately 1 m. The imaging detector consisted of radiation resistant optics (two Hasselblad lenses (focal distance = 100 mm) in tandem-arrangement), a single-crystal scintillator (Ce-doped $Lu_3Al_5O_{12}$ (LuAG:Ce) by Crytur, Czech Republic) and the ESRF in-house-developed CCD camera FReLoN camera (type: 2K, 2048 × 2048 pixels, 14 μm pixel size) [66,67]. The effective pixel size is 13 μm and the max. field of view is 26 mm × 26 mm, limited by the beam height of around 13 mm. In order to encompass the complete specimen, the detector's field being substantially smaller than the sample lateral size, 360 degree scans were carried out with the axis of rotation shifted to the edge of the field of view. This allows stitching projections and hence, creates 180 degree scans with increased lateral field of view. Several tomographic scans were merged vertically.

We adopted two methods to quantify the pebbles contacts: the first one is a volume segmentation algorithm based on the watershed thresholding and run over the Euclidean distance map [68], and the second is that developed by Aste [25,26].

In both methods one first has to determine the pebble centres. The identification is based on the maximal balls inscribed in the respective pebbles (solid phase) [69]. Two maps are generated by this operation, the first one assigns to each voxel the radius of the largest inscribed ball as the granulometry operator generates it. The second map is the set of identifiers of the centres of the maximal inscribed balls. To compute the inscribed spheres radius, we used the exact Euclidean distance map and a priority queue [70]. All the voxels of the solid phase are pushed into the priority queue according to their shortest distance to the pore space. The voxels v with the highest priority (highest distance) are firstly removed from the queue and their distance r_v (expressed as an integer number) to the nearest pore is attributed to every voxel of the ball centred on v and having radius r_v. The identifiers map is generated at the same time using a unique identifier generated from the coordinates of v. A ball is said to be maximal if the number of voxels with the same ball identifier corresponds approximately to the theoretical volume of the known ball radius. In the present study only one maximal ball could be accommodated in each pebble. Partial balls may be detected due to either the discretisation or if pebbles are not perfectly spherical. The maximal ball centres are then used as markers for the watershed-based segmentation and for the contact analysis carried out through the method developed in [33].

From the pebble segmentation, generating the pebbles adjacency graph is straightforward: one simply scans the segmented pebble map and connects pebbles that have at least one neighbouring voxel (in 6-connexity). Whilst the maximal ball extraction is not very sensitive to the threshold used to separate solid and pore phases (at least for small deviations from the threshold's confidence value), the contact estimation via any segmentation method is highly dependent on the voxel size and on the chosen threshold. The threshold variations near the threshold confidence value only affect voxels on the first voxel layer of the pebble surface. Thus, a lower threshold could artificially disconnect two pebbles touching each other and, conversely, a higher threshold could generate a false connection between two disjointed pebbles. In the present case, the threshold was chosen to fit the experimental porosity value (confidence value). Table 1 summarises some characteristics of the scanned samples. An important quantity with regard to CT accuracy is the sphere diameter expressed in voxel sizes. The values listed in Table 1 are significantly larger than those in [26] where the value was 32 voxels.

Table 1
Characteristic CT values.

Exp.	No of spheres	Voxel size (mm)	d (voxel size)
A	39,895	0.048	49
B	40,826	0.048	49
C	4854	0.048	49
D	7402	0.013	182
E	16,348	0.013	182

4. Results

4.1. Selected experiments

The selected five examples (Exp. A, Exp. B, Exp. C, Exp. D, Exp. E) do not claim to be representative for maximum packing fractions but exhibit very characteristically differing packing structures, see Table 2.

In all experiments, except Exp. D, the Plexiglas containers were filled gently in one step with all spheres before the onset of densification.

In Exp. A, the container was moderately densified for about 10 s by tapping, knocking gently against the container walls and turning the closed container upside down, similar to the procedure used by [6,18,25,26]. The aim of this experiment was to avoid the build-up of large regular wall zones and to generate a RCP in the remainder volume.

For Exp. B, as predecessor Exp. A was used and vibration was applied. Granular convection was suppressed by vibration with restricted amplitudes, see Section 4.2.

In Exp. D, about half of the spheres were filled in and vibrated with a free particle surface. After adding the second half of the spheres (*2 step filling*), the system was vibrated further with a free particle surface. (In later experiments, similar packing structures and packing fractions were also obtained by *1 step filling*.)

For Exps. C, D, and E, stiff packing structures built up at the end of the first vibration cycle.

Before discussing in detail the results shown in Fig. 4, some aspects of granular convection are addressed.

4.2. Role of granular convection in respect to crystallisation

In general, packed beds become increasingly fluidic, i.e. favouring granular convection, by increasing the vibration parameters, and D/d or H/d. In our experiments, for D/d < 20 no granular flow was observed for H/d < 20. For H/d > 20, an initial granular convection could occur which came to rest after some time. The range D/d < 20, H/d > 20 is characteristic for radially dominated crystallisation, cf. also [22], see Exps. C and E in Fig. 4.

For D/d ≈ 34, the experiment from [21] with H/d ≈ 16 is well suited for comparison because both the vibration and packing geometry parameters are in the same range. For Γ ≈ 3 and a/d ≈ 0.13, a hexagonal packing area occurred on the top after ≈5 min which increased with time in size, resulting finally in $\gamma_t = 0.658$. In contrast to [21], an initial convection roll was not observed. For smaller Γ and a/d values, however, convection rolls, axisymmetric or with inclined axis, occurred frequently if the container was not centred correctly which corresponds to the findings from [61].

For large D/d, the instability toward convection increases significantly with increasing H/d. For D/d ≈ 34, H/d ≈ 28, Γ ≈ 2.3, and a/d ≈ 0.05, an initially present axisymmetric convection roll came to rest after some minutes for an optimum container position. Then, with increasing time, an almost perfect hexagonal packing developed at the cylinder wall, connected with sphere arrangements in form of rings at the packing surface, most expressed close to the cylinder wall. Shortly later, hexagonal islands appeared at the surface close to the cylinder axis, and, characteristically, significant granular convection emerged in the outward annular zone, destroying the regular radial structure at the cylinder wall. This effect was always observed when

Table 2
Experimental parameters and packing fraction results; d = 2.34 mm.

Exp.	D (mm)	D_i (mm)	H (mm)	D/d	Di/d	H/d	/D	a/d	Γ	$\gamma_{t-\ nom}$	γ_{t-CT}	$\gamma_{t-CT}/\gamma_{t-CTnoncorr}$	$\gamma_{t-nom}/\gamma_{t-CT}$
A[a]	78.5	3.0	87.1	33.5	1.30	37.2	1.10			0.624	0.618	0.982	1.009
B[b]	78.5	3.0	87.1	33.5	1.30	37.2	1.10	<0.23	<3	0.638	0.642	0.994	0.994
C	30.2	–	70.2	12.9	–	30.5	2.30	0.08	2.0	0.635	0.628	0.995	1.011
D[c]	50.4	–	39.1	21.5	–	16.7	0.78	0.12	2.8	0.666	0.668	0.986	0.997
E[d]	49.1	–	87.0	21.0	–	37.2	1.77	0.12	2.8	0.656	0.658	1.004	0.997

[a] Tapping.
[b] Amplitude-limited vibration.
[c] 2step filling.
[d] Vibration with free surface.

the crystallisation, starting on the bottom plate, finally extended over the largest fraction of the packed volume, cf. Exp. D in Fig. 4. If in this situation Γ was reduced, γ_t increased, as measured also by [22]. The probable reason for this was that the arrangement close to the cylinder wall became more ordered again without influencing remarkably the axial crystallisation zone.

The larger H/d at D/d = 34, the more difficult it became to reach a steady state condition where initial convection came to rest. For the maximum H/d (H/d ≈ 38), a steady-state situation was no longer reached. Because granular convection hinders primarily the effective crystallisation at the cylinder wall, the resulting packing fractions were <0.64. An increase of γ_t was only achieved by suppressing granular convection by successively tightening the top lid. In this way, large vibration energies could be applied in combination with limited amplitudes.

It is found that inner cylinders stabilise the packings; for D/D_i = 80/20, no convection was observed for all H/d values.

4.3. Void fraction distributions

The accurate CT measurement of the void fraction at the wall, ε = 1, is difficult to achieve owing to the large void fraction gradient, the finite pixel size, the tolerances affecting the cylinder diameter, and the eccentricities between cylinder axis and axis of revolving table, see also [44]. Therefore, the data referring to regions close to the walls were corrected using the void fraction relation for spheres at plane walls [17], deduced from geometrical considerations, given by

$$\varepsilon = 1-(1-\varepsilon_{1min})/0.907\left(2\pi/3^{0.5}\right)\left(x-x^2\right), \quad (1)$$

where x is wall distance normalised to d and ε_{1min} is the measured value of the void fraction minimum at x = 0.5. The term $(1-\varepsilon_{1min})$ is also designated as wall coverage. For hexagonal dense packing, this value is 1 − 0.093 = 0.907; in general, this value is significantly smaller. The corrected CT results, $\gamma_{t\text{-}CT}$, are considered to be more accurate than the non-corrected values, $\gamma_{t\text{-}CTnoncorr}$, and will be used in the following. The packing fraction differences between nominal values and corrected CT values are at maximum 1%, see Table 2.

Following the procedure introduced previously [43,47], the total packing volume is divided in different subzones:

A) *d/2 wall layer zone and inner zone*: The void fraction of the total packing volume ε_t is composed of the volume void fractions $\varepsilon_{d/2\ n}$ in the different d/2 layers, along with corresponding volumes $V_{d/2\ n}$ and the volume void fraction in the remaining inner volume ε_i:

$$\varepsilon_t = \left(\Sigma\varepsilon_{d/2\ n}V_{d/2\ n} + \varepsilon_i V_i\right)/V_t. \quad (2)$$

The above relationship is useful to determine ε_i with the generally known value ε_t. In the present experiments, the $\varepsilon_{d/2}$ contributions of all individual walls were directly measured. For $\varepsilon_i < \varepsilon_{RCP} \approx 0.36$, respectively, $\gamma_i > 0.64$, structured packings are expected to play an increasing role. As shown in Table 3, in all experiments, except Exp. A, γ_i is larger than 0.64.
In general, $\varepsilon_{d/2}$ is obtained by integration of Eq. (1) over x = 0 and 0.5 which results in $\varepsilon_{d/2} = 1 - (2/3)(1-\varepsilon_{1min})$. For a hexagonal wall layer, $\varepsilon_{d/2}$ has the minimum value of ≈0.4. The wall coverages depend on D/d and wall orientation; at the top plate the values are generally smaller than at the bottom plate; first results were given in [47]. More detailed analyses will be the subject of a future paper.

B) *Inner radial volume, inner axial volume*: In general, radial and axial void distributions (RVD and AVD, respectively), are determined using the total packing volume. For the RVD this means that the void fractions in the top and bottom wall zones, cf. Fig. 2, are also included in the evaluation. For the volume without these two wall zones, designated as inner axial volume, $V_{i\text{-}ax}$, the RVD is representative for an infinitely long cylinder (no end effects, d/H = 0 according to [6,18]), therefore, this RVD is termed "L∞". Correspondingly, the AVD evaluated with the inner radial volume, $V_{i\text{-}rad}$, not including the cylinder wall zones, is designated as "D∞" because it is more representative for the packing between two plane walls. Fig. 4 shows these inner volumes which can be only defined if the respective wall zones are separated. In the case that both the axial and radial wall zones are clearly separated, a random packing exists in the "bulk zone". The packing fractions of the different zones are listed in Table 3.

The AVDs and RVDs in Fig. 4 are evaluated both within the total volumes and, for separated wall layers, also within the corresponding inner volumes. In Exp. A (moderately densified sample), void fluctuations are damped out at the outer cylinder wall (designated as concave, cc, wall) after ≈5 wavelengths. It should be recalled that for hexagonal densely packed structures one wavelength corresponds to a thickness of ≈0.82d; at the cc wall slightly larger values were measured. At the flat top and bottom plates and at the convex, cv, inner cylinder wall ≈4 wavelengths are observed; a large bulk zone exists in between. In this case, γ_b is close to γ_{RCP}.

In Exp. B, the regular structures at the cc wall and the bottom plate are significantly more developed compared to Exp. A. The regular structure at the top plate is less expressed than at the bottom plate because gravity promotes regular bottom structures both during filling and vibration. All wall zones appear still to be separated but the zone in between is much smaller than in Exp. A. The small fluctuations in this zone, however, indicate that a "pure" random packing no longer exists. This is also confirmed by the value for γ_b which is larger than γ_{RCP}, see Table 3. In many other experiments with inner cylinders, not presented in this article, the cc and cv wall zones are strongly interconnected.

In Exps. C–E, no inner cylinders were used. Exp. C is representative for cylindrical containers with H/d > 1 and a small D/d value. A radially dominated regular structure exists in the total cross section. An inner radial volume according to the definition above does not appear. Analysing in more detail the fluctuations of the AVD, it proves that they originate from the well-developed radial oscillations.

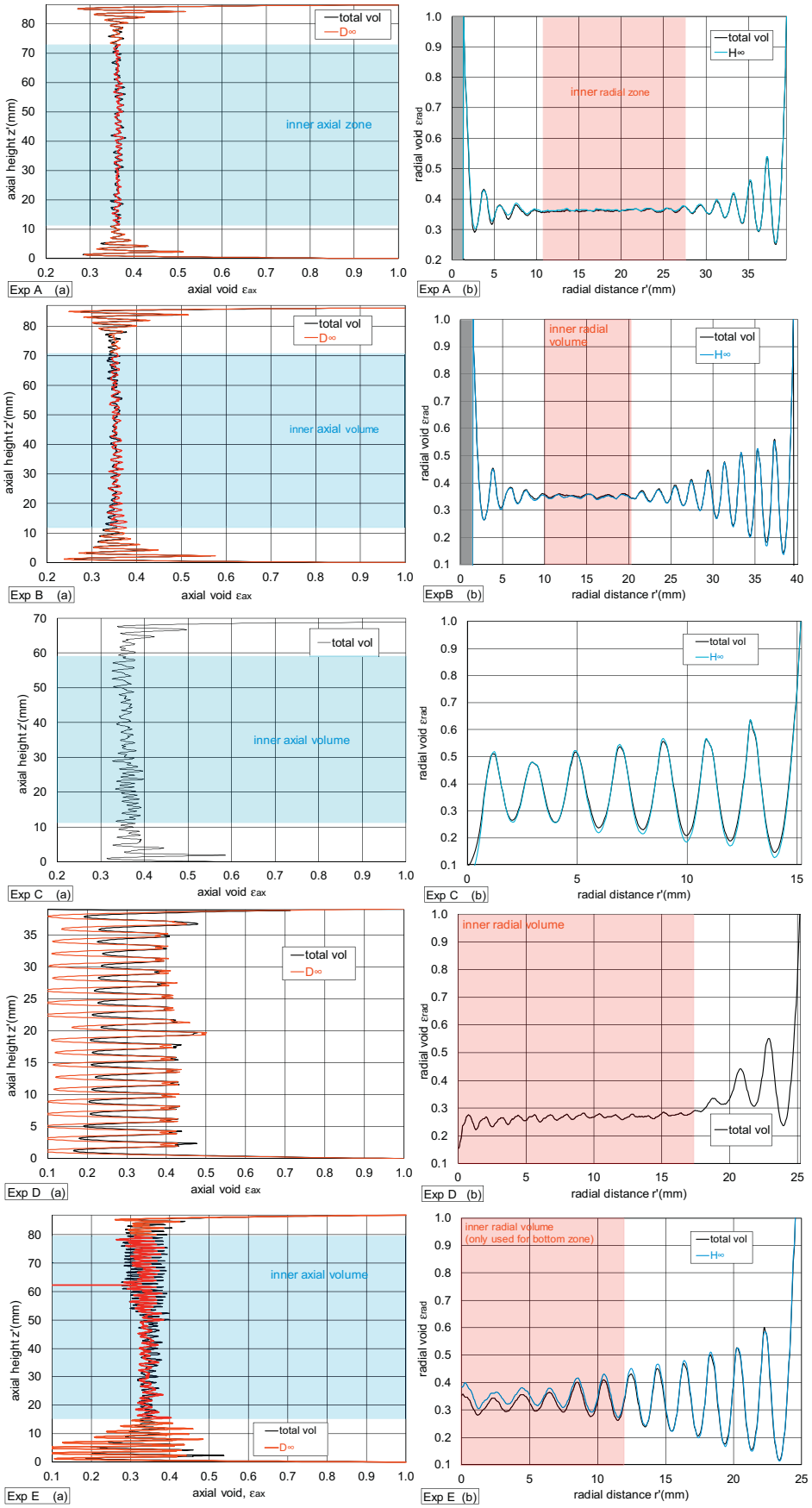

Fig. 4. AVDs (a) and RVDs (b) for Exps. A–D, cf. Table 2.

Table 3
Zone packing fractions.

Exp.	$\gamma_{t\text{-}CT}$	$\gamma_{d/2}$	γ_i	$\gamma_{H\infty}$	$\gamma_{D\infty}$	γ_b
A	0.618	0.468	0.634	0.636	0.634	0.635
B	0.642	0.466	0.652	0.650	0.647	(0.650)[a]
C	0.628	0.499	0.653	0.633		
D	0.668	0.559	0.687		0.731	
E	0.658	0.536	0.675	0.649		

[a] No longer pure random packing.

Exp. D is characteristic for cylinders with H/D ≤1. In this case, crystallisation has started from the bottom plate and persists over the total packing height. The cc wall zone is less regular than in the other experiments because of the influence of the dominating axial structure. The AVD for the inner radial volume shows a much larger regularity than the AVD evaluated for the total volume. The packing fraction $\gamma_{D\infty}$ is quite close to the maximum value of 0.74 for hexagonal dense packing, see Table 3.

The vibration effect on a sample with a free particle surface is shown in Exp. E: A regular structure has built up from the bottom plate with a thickness of about 7 wavelengths. Above this region, the radial structure is increasingly prevailing in the cross section. The regular structure at the top plate is not well-developed. The fluctuation of the AVD in the upper part originates also from the radial oscillations. For Exp. E, an inner radial volume can be only defined for the bottom zone. Here, large differences in the AVD are observed.

Details of packing structures can be better demonstrated by using results from the inner radial or axial volumes, therefore, the following analyses are based on the related data.

Figs. 5–6 show void distributions as a function of the dimensionless wall distance x. Fig. 5 compares AVDs at the flat bottom plates: the curve for Exp. D is close to that for perfect hexagonal packing ($\varepsilon_{min} = 0.09$, layer distance 0.817d). The double peaked void maxima were clearly measured for the first time. They result from the coexistence of two neighbouring sphere layers, as calculated first by [17]. In Exp. E, the large regularity of the first layer decreases with increasing x.

RVDs for cc walls are summarised in Fig. 6: For Exps. B, C, and E, the wall layer void fraction minimum indicates that an almost dense hexagonal packing exists. However, double peaks, are not measured. Because of wall curvature, the contact points with the second wall layer must shift radially inwards and by that, the first void minimum should shift to x > 0.5 [14]. In practice, there are other effects which can compensate for this effect, as already stated in [17]. The reason for the stronger decay of regularity in the vicinity of cc walls compared to packings at flat walls is discussed in detail in Section 4.4.

In respect to convex wall layers, only the result for Exp. B with $D_i/d = 1.3$ is presented, see Fig. 4. For this value, the fluctuations damp out after a small wall distance. In other experiments, not shown here, the increase of the cv wall zone with increasing D_i/d was measured.

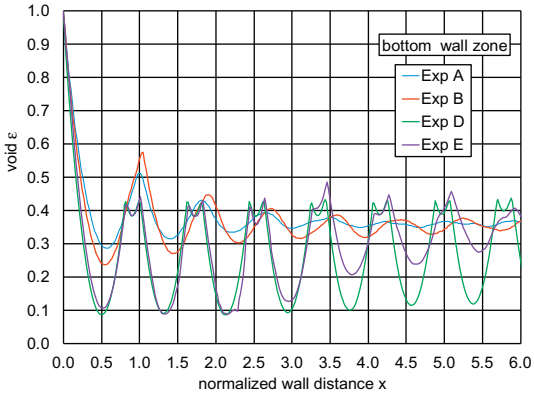

Fig. 5. AVDs ($V_{i\text{-}rad}$) at plane bottom walls.

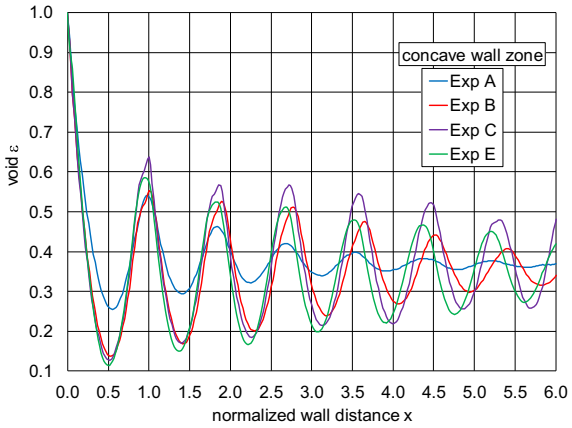

Fig. 6. RVDs ($V_{i\text{-}ax}$) at cc cylinder walls.

This section has demonstrated that wall fluctuations must not damp out as fast as previously assumed [14,34]. The development of a more comprehensive correlation remains a challenge for future work.

4.4. Wall layers

The regular layers at transparent cylindrical walls have attracted many researchers and have given rise to speculations on how these structures continue inwards. For tapped sphere beds, only small regular zones are observed, see Fig. 7(a). After the onset of vibration, regular structures form fast at the cc wall and a state can be reached where almost all wall spheres are arranged in a hexagonal dense layer. Fig. 7(b) shows such an arrangement with "horizontal sphere chains", which preferably start to build up from the bottom. In an early work [8] it was assumed that owing to gravitational stability, the vertical positions of the spheres in the next wall layers are the same as in the 1st cc layer. This structure was designated as double-nested [8] or tetragonal-sphenoidal [16] with a packing fraction of 0.698. The existence of hexagonal dense packings according to the fcc or hcp structure (see below) was excluded because of the gravitational instability.

For free surface vibration and cylindrical containers with H/D ≫ 1, the occurrence of "vertical sphere chains" is also characteristic. Zones with both types of sphere chains are often observed, as well as other oblique chains due to vibration asymmetries. Exp. E is an example where the two distinguished structures coexist, see Fig. 7(c). However, with further vibration, the zones with vertical sphere chains tend to shrink and eventually the total cc wall can be covered by a dense hexagonal array of horizontal sphere chains.

Selected sphere layers can be simply visualised by plotting the CT sphere centre coordinates, cf. Fig. 2, in a chart with z′ and the cylinder angle φ as coordinates. Circles with diameters equal to the sphere diameter are used as symbols.

Fig. 8 shows a portion of the cc wall region of Fig. 7(c) with vertical sphere chains. In the upper part, sphere positions of the 1st and 2nd wall layer are plotted. The spheres of the 2nd layer in the column below the sphere A fit in the interstices between three neighbouring spheres of the 1st layer, corresponding to a locally hexagonal dense lattice. With increasing wall distance, the radius decreases on which subsequent sphere centres are located. Therefore, 2nd layer spheres in the columns adjacent to A are shifted to positions where locally a hexagonal dense packing is no longer possible. For the column B, a position is reached where the 2nd and 1st layer spheres are arranged in an orthorhombic structure. The 2nd and following cc wall layers can therefore be considered as mixtures of hexagonal dense and orthorhombic structures. This is confirmed by the positions of the spheres of the 3rd cc layer, shown in the lower part of Fig. 8.

For horizontal sphere chains at the cc wall, see lower part of Fig. 7(c), the structure in the subsequent layers is similar to that outlined in Fig. 8,

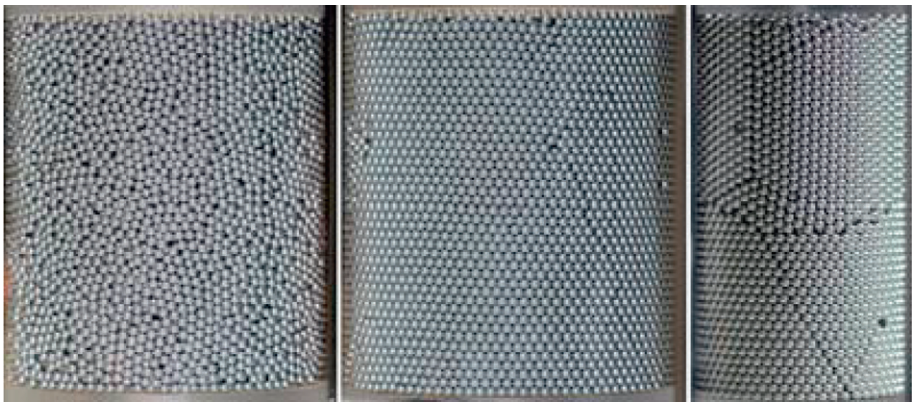

Fig. 7. Photographs of cc cylinder wall layers.

i.e. a double-nested or tetragonal-sphenoidal packing according to [8] has no relevance in our experiments.

Fig. 9 shows sphere layers for the bottom zone of Exp. D. Except for the spheres close to the cylinder wall, a hexagonal dense sphere arrangement exists in the 1st layer, labelled as Type A. The spheres of the 2nd layer (Type B) are located in the interstices of the 1st layer. The spheres of the 3rd layer can be arranged either as Type A or, as it is the case in Fig. 9, fill the other available interstices (Type C). The repeating sequences AB or ABC correspond to the hexagonal close packed, hcp, crystal structure, and the face centred cubic, fcc, crystal structure, respectively [20]. In sphere packings above horizontal plates, random sequences are expected; and the term dense hexagonal packing used in this work refers to the case of arbitrary sequences. In all cases the packing fraction is 0.74 and the coordination number N_c is 12.

4.5. Contact angles

Regular packing patterns are also reflected in characteristic distributions of the contact positions on the spheres, expressed by the poloidal contact angle ϑ, starting at the North Pole, and the azimuthal angle ψ [41,43]. For spheres above the bottom plane, ψ is defined using a fixed Cartesian x′-y′ system; for spheres close to cylinder walls, ψ starts perpendicular to the radial vector, see Fig. 10. Contacts between Plexiglas walls and aluminium spheres were not measured by CT, hence, only contacts with other spheres are presented. Frequencies for 10° groups are shown in Figs. 11–13. For the poloidal angle, the frequency was normalised by the corresponding surface increment. For the 1st cc wall layer of Exp. B, Fig. 11, sharp "crystallinity" peaks at $\vartheta \approx 30°$, $\approx 90°$, and $\approx 150°$ are present, cf. Fig. 7(b). With increasing layer number, the peaks become weaker and for the bulk zone a rather homogeneous distribution is found. The azimuthal angle for the 1st cc layer has strong peaks at $\psi \approx 0°$ and 180° but no peaks appear in between, Fig. 12. A number of peaks, generated by second layer spheres, are observed between 230° and 320°. Again, a flat distribution is obtained for the bulk zone.

For the dense hexagonal packing in the bottom zone of Exp. D, outstanding poloidal peaks occur, as expected, at $\vartheta \approx 35°$, 90° and 145°. Regarding ψ, Fig. 13, in the 1st layer there are six contacts from neighbouring 1st wall layer spheres, separated from each other by 60°, and additionally, displaced by 30°, three contacts originating from 2nd layer spheres, separated by 120°. The second layer has 3 more contacts. These corresponding ψ values are relevant for the ABC stacking.

4.6. Coordination numbers

The determination of coordination numbers N_c from experiments encounters problems because of the finite spatial resolution (in CT

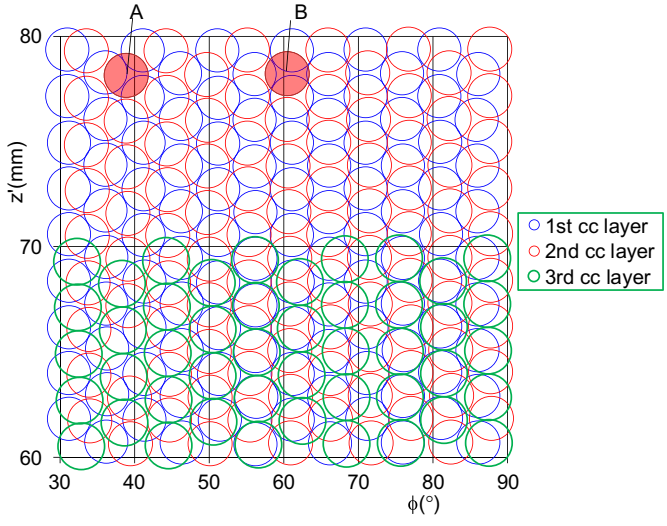

Fig. 8. Upper portion of Fig. 7(c): 1st, 2nd and 3rd wall sphere layer.

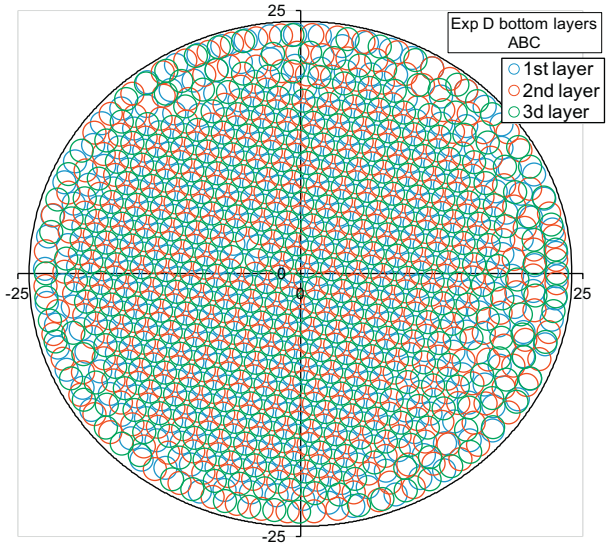

Fig. 9. Exp. D: bottom zone sphere layers.

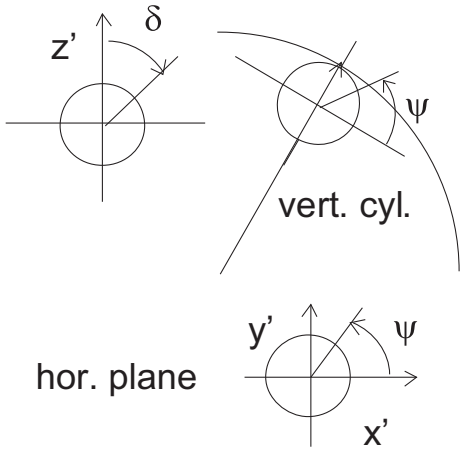

Fig. 10. Definitions of poloidal and azimuthal angles.

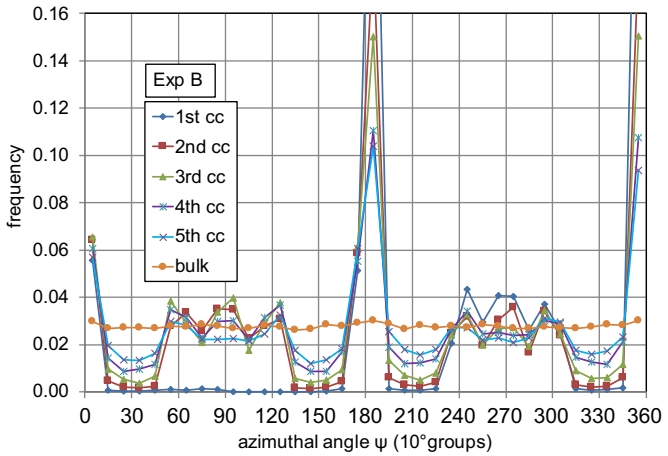

Fig. 12. Exp. B: Azimuthal angle distribution ($V_{i\text{-}ax}$) for cc wall zone.

measurements: the voxel size), as well as deviations from the nominal sphere diameter. This results in uncertainties with respect to sphere positions and diameters which might affect the correct evaluation of N_c. This issue was tackled in detail by [25], where a computational method was used based on the uniform expansion of the spheres. For a diameter value of slightly larger than 1.02d a good agreement was obtained with previous results from literature. Later on, a more sophisticated method was applied [26], resulting in effective d-values slightly above the previous ones.

With the watershed algorithm (see Section 3.2), N_c is determined directly. The bulk zone of Exp. A is suited to compare our method with those from [25,26], because of similar packing fractions close to γ_{RCP}, see Table 3. Our results agree well (not shown in this article) with those from [26] for an expanded diameter of 1.05d, thus giving confidence in our evaluated N_c values for other cases.

For the RCP, N_c was experimentally determined to be ≈ 7 [26], whereas N_c must be 12 for hexagonal dense packings, except for the first wall layer, where $N_c = 9$. The N_c distribution close to cc walls was first investigated by [31] and, apart from the first layer, N_c was ≈ 8, independent from wall distance. Again, it should be reminded that previous measurement techniques were associated with larger uncertainties.

For the well-ordered cc wall zone of Exp. B, Fig. 14, N_c peak values of 7 and 8 are obtained for the 1st and 2nd cc layer, respectively. For the other layers, as well as for the zone in between the wall zones, $N_c \approx 7$.

Fig. 15 presents N_c results for the inner volumes of Exp. D: in the large regular structure in the bottom region, $N_c = 12$ and no remarkable differences exist for the different layers, with the exception of the 1st layer with $N_c = 9$. Much less regular is the packing in the 1st layer of the cc wall.

4.7. Radial distribution function

The radial distribution function (RDF) is the probability of finding one particle centre at a certain distance r (distance normalised by the sphere radius) from the centre of a given particle, defined by

$$\mathrm{RDF}(r) = \Delta N(r) / \left(4\pi r^2 \Delta r \rho_0\right), \tag{3}$$

where $\Delta N(r)$ is the number of sphere centres situated at a distance between r and $r + \Delta r$ from the centre of a given sphere and ρ_0 is the average number of particles per unit volume in the packing. The RDF has been used first by [9] using experimental data and has become a standard tool for DEM simulations. For the CT experiments in [25] the RDF was calculated for RCP. Our result for the bulk zone of Exp. A, not shown in this article, agrees very well with those in [25].

Results for the bottom zone of Exp. D, Fig. 16, show first large peaks for $r = 1, \sqrt{2}, \sqrt{3}$. For layers with ABC stacking sequence (fcc crystal), less peaks appear compared to the ABA sequence (hcp crystal), e.g. a peak at $r = 1.91$ exists only for the ABA sequence. This peak occurs first in the 5th layer, consequently, the sequence ABCABA must exist. This could be also confirmed by plotting the sphere positions in the corresponding layers according to Section 4.3.

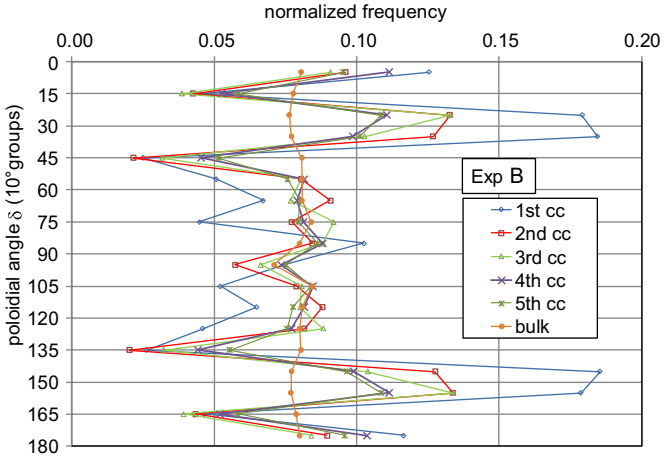

Fig. 11. Exp. B: Poloidal angle distribution ($V_{i\text{-}ax}$) for cc wall zone.

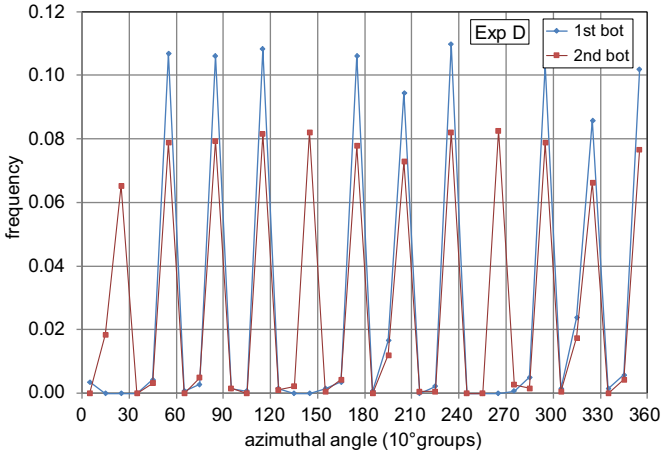

Fig. 13. Exp. D: Azimuthal angle distribution ($V_{i\text{-}rad}$) for bottom wall zone.

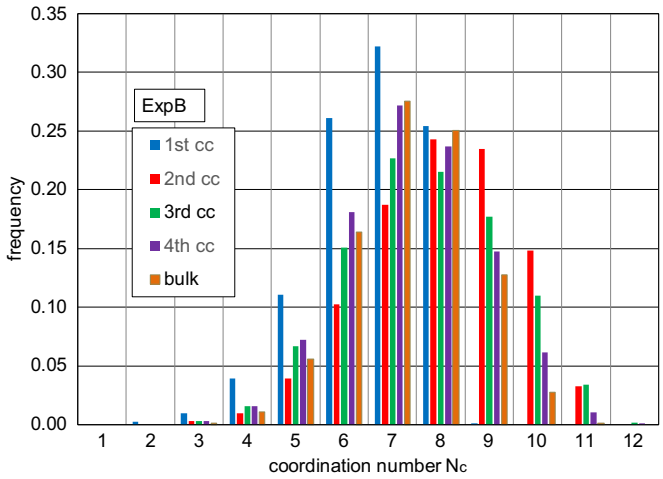

Fig. 14. Exp. B: Coordination number distributions ($V_{i\text{-}ax}$) for cc wall zone and bulk.

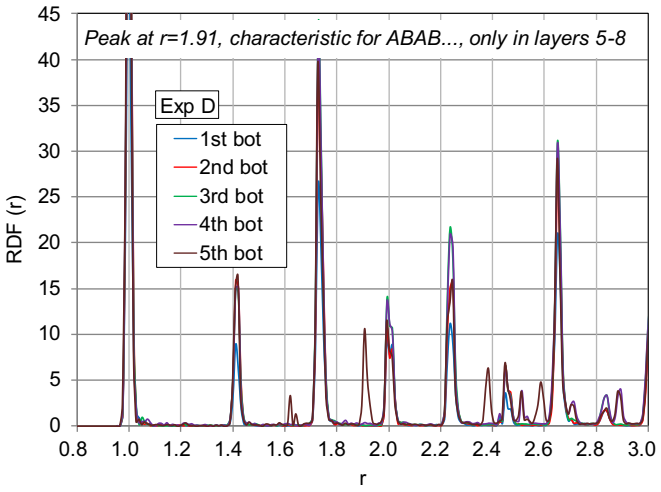

Fig. 16. Exp. D: RDF for bottom zone, ($V_{i\text{-}rad}$).

For the cc wall zone of Exp. B, Fig. 17, already the RDF for the 1st layer displays much less details compared to Fig. 17. This is another proof that the regularity of the 2nd layer is already considerably perturbed. With increasing wall distance, the peaks become even smaller and the curve for the bulk zone agrees again fairly well with that from [25] for RCP. Compared to angle distributions, the RDF appears to be less sensitive for characterising regular structures.

4.8. Voronoi cell packing fractions

There are several other measures to quantify order/disorder of packings [50–51]. Voronoi tessellation is one of the frequently used methods. For a packing of mono-sized spheres the Voronoi cell is the polyhedron that contains all points closer to a given sphere centre than to any other. Voronoi tessellation partitions the whole space of a packing unequivocally into a set of Voronoi cells.

Fig. 18 shows the Voronoi cell packing fraction, defined as the sphere-to-cell volume ratio. For the 1st cc layer the Voronoi packing fraction cannot be very large because the wall is one side of the polyhedron, which results in rather large cells. For the 2nd cc layer the packing fraction is remarkably larger than the bulk value, which reflects better the influence of ordered structure. Farther from the wall, the packing factors approach the bulk value, shown also in the figure legend by listing the mean packing fractions. Although Voronoi tessellation appears to be not better suited to characterise the degree of structure regularity than other measures presented before, the advantage is the determination of packing fractions of individual sphere layers which is important for the flow distribution in systems with fluid flow.

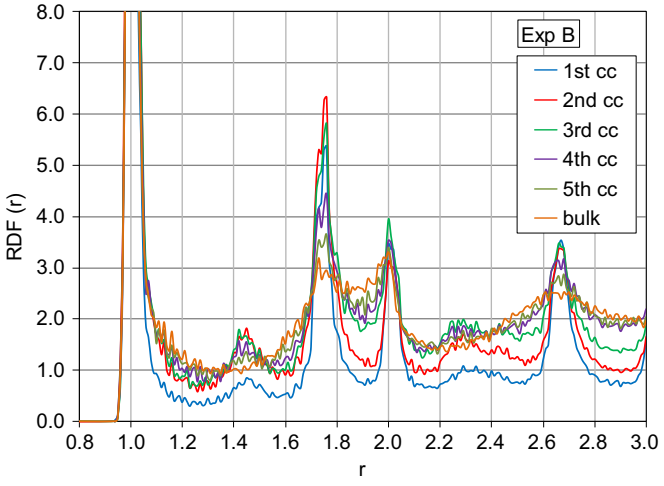

Fig. 17. Exp. B: RDF for cc wall zone, ($V_{i\text{-}ax}$).

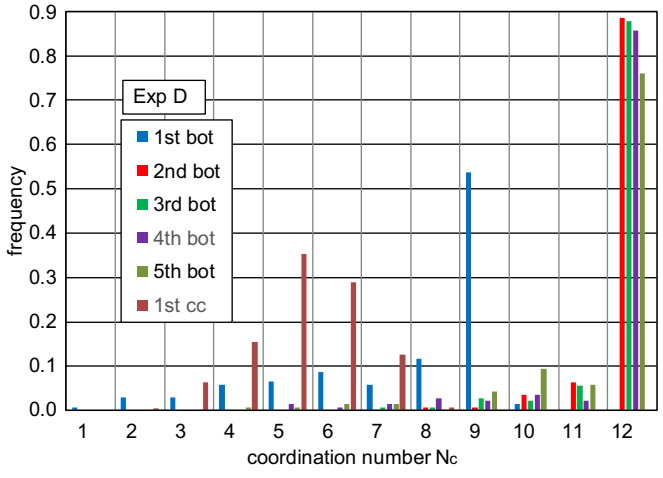

Fig. 15. Exp. D: Coordination number distributions for bottom wall zone ($V_{i\text{-}rad}$) and 1st cc layer ($V_{i\text{-}ax}$).

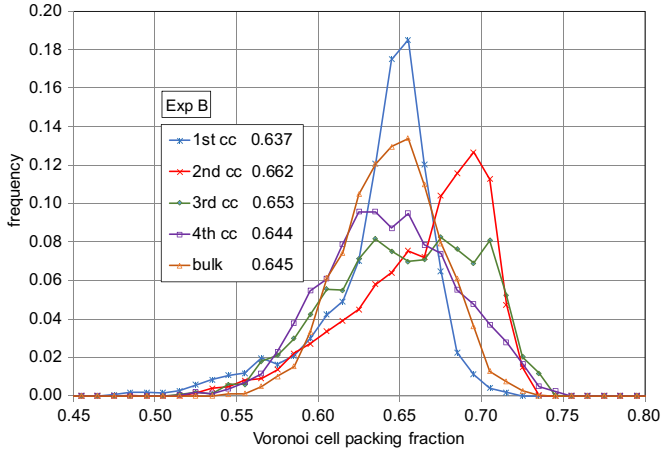

Fig. 18. Exp. B: Voronoi cell packing fractions for cc wall layers and bulk zone, ($V_{i\text{-}ax}$).

5. Conclusions

Advanced X-ray computed tomography has demonstrated to be well suited for the measurement of local structures of mono-sized sphere packings in cylindrical containers with and without inner cylinders. Five experiments with specifically differing packing structures have been analysed.

The development of regular structures depends on geometric parameters (main variables: d, D, D_i and H), filling mode (one step filling, batch-wise or continuous filling), and vibration mode (free/restricted particle surface, vibration parameters Γ and a/d). The total packing fraction γ_t is also dependent on these parameters and the large scattering of measured data reported in literature reflects the complex interaction of the parameters.

The existence of significant regular structures can be assessed by calculating the packing fraction in the inner container volume which is the total volume minus the volume of the wall layers with d/2 thickness.

Structural features in the packings in the proximity of concave, flat and convex walls were analysed by means of void fraction distributions, sphere centre positions, contact angle distributions, coordination numbers, radial distribution function and Voronoi cell packing fractions. The combination of these tools provides a comprehensive understanding of structural details.

The increase of container packing fractions by using appropriate vibration parameters is caused by the growth of structured packings in wall zones, as demonstrated by two experiments with the same geometric parameters.

For cylinders with a height to diameter ratio $H/D \gg 1$, ordered configurations build up preferentially in radial direction starting from the hexagonally ordered layer at the concave wall. Depending on D/d, regular zones can persist throughout the total cross section. For $H/D < 1$ and $D/d \gg 1$, hexagonal dense structures grow preferentially from the flat bottom plate and can dominate the total container volume.

Only at flat walls ($D/d = \infty$), hexagonal dense packings can grow and persist in a large volume fraction. At curved walls, the regularity must progressively decrease away from the wall, as demonstrated by visualising sphere centre positions and confirmed by employing the analytical tools mentioned above.

The role of granular convection on the crystallisation process has been addressed and deserves further attention in future investigations.

Previous statements that the thickness of wall zones is about (4–5)d cannot be generalised to mono-sized sphere packings. The elaboration of a generalised correlation for void fraction distributions is still a pending task.

Only a few characteristic results were presented; special topics going beyond the scope of this article will be addressed particularly in forthcoming publications.

Nomenclature

a	vibration amplitude (m)
d	sphere diameter (m)
D	outer (concave) container diameter (m)
D_i	inner (convex) cylinder diameter (m)
g(r)	radial distribution function RDF
f	frequency (s^{-1})
H	cylinder height (m)
N_c	coordination number
r	distance between spheres divided by d
r′	radial coordinate (m)
V_b	bulk volume (m^3)
$V_{d/2}$	volume of d/2 wall layers (m^3)
V_i	inner volume = $V_t - V_{d/2}$ (m^3)
$V_{i\text{-}rad}$	inner radial volume = volume between radial wall layer zones (m^3)
$V_{i\text{-}ax}$	inner axial volume = volume between axial wall layer zones (m^3)
V_t	total packing volume (m^3)
w′	width of prismatic container (m)
x	wall distance divided by d
x′	horizontal coordinate (m)
y′	vertical coordinate (m)
z′	axial coordinate (m)

Greek symbols

ε	void fraction or porosity
δ	polodial contact angle
γ	packing fraction
Γ	vibration intensity
ω	angular frequency
φ	cylinder angle
ψ	azimuthal contact angle

*Abbreviations*AVD
axial void distribution

cc	concave
cv	convex
CT	computed tomography
DEM	discrete element method
RDF	radial density function
RVD	radial void distribution
D∞	container without cylinder wall effects
H∞	container without axial wall effects
1sf	one step filling

Acknowledgements

The work was funded by Fusion for Energy (F4E-FPA-380:SG01). Special thanks go to L. Brinkschulte from KIT-FAST for the support of accelerator measurements.

References

[1] S. Whitaker, Heat and mass transfer in granular porous media, Adv. Dry. 1 (1980) 23–61.
[2] F. Gritti, G. Guiochon, Mass transfer kinetics band broadening and column efficiency, J. Chromatogr. A 1221 (2012) 2–40.
[3] A. Koster, H.D. Matzner, D.R. Nichols, PBMR designs for the future, Nucl. Eng. Des. 222 (2003) 231–245.
[4] F. Cismondi, B. Kiss, F. Hernandez, E.N. Diaye, G. Legradi, J. Reimann, M. Ili, The fundamental role of fluid dynamic analyses in the design of the solid EU Test Blanket Module, Fusion Eng. Des. 87 (2012) 1123–1129.
[5] A. Westman, H. Hugill, Packing of spheres, J. Am. Ceram. Soc. 13 (10) (1930) 767–769.
[6] G.D. Scott, Packing of equal spheres, Nature 188 (1960) 908–909.
[7] J.C. MacRae, W.A. Cray, Br. J. Appl. Phys. 12 (1961) 164.
[8] R.K. McGeary, Mechanical packing of spherical particles, J. Am. Ceram. Soc. 44 (1961) 513–522.
[9] G.D. Scott, Radial distribution of the random close packing of equal spheres, Nature 194 (1962) 956–957.
[10] R. Jeschar, Druckverlust in Mehrkornschüttungen aus Kugeln, Arch. Eisenhüttenwes. 35 (Heft 2) (1964) 91–108.
[11] J.E. Ayer, F.E. Soppet, Vibratory compaction I. Compaction of spherical shapes, J. Am. Ceram. Soc. 48 (1965) 180–188.
[12] T.G. Owe Berg, R.L. McDonald, R.J. Trainor, The packing of spheres, Powder Technol. 3 (1969/70) 183–188.
[13] L.H.S. Roblee, Radial porosity variations, AICHE J. 4 (1958) 460–464.
[14] R.F. Benenati, C.B. Brosilow, Void fraction distribution in beds of spheres, AICHE J. 8 (1962) 359–361.
[15] M.C. Thadani, F.N. Peebles, Variation of local void fraction in randomly packed beds of equal spheres, Ind. Eng. Chem. Process. Des. Dev. 5 (1966) 265–268.
[16] K. Ridgway, K.J. Tarbuck, Radial voidage variations in randomly-packed beds of spheres of different sizes, J. Pharm. 18 (1966) 168–175.
[17] K. Ridgway, K.J. Tarbuck, Voidage fluctuations in randomly-packed beds of spheres adjacent to a containing wall, Chem. Eng. Sci. 23 (1968) 1147–1156.
[18] R.P. Zou, A.B. Yu, The packing of spheres in a cylindrical container — the thickness effect, Chem. Eng. Sci. 50 (1995) 1504–1507.
[19] J.B. Knight, C.J. Fandrich, C.N. Lau, H.M. Jaeger, S.R. Nagel, Density relaxation in a vibrated granular material, Phys. Rev. E 51 (5) (1995) 3957–3963.
[20] O. Pouliquen, M. Nicolas, P.D. Weidman, Crystallization of non-Brownian spheres under horizontal shaking, Phys. Rev. Lett. 79 (19) (1997) 3640–3643.

[21] L. Vanel, A.D. Rosato, R.N. Dave, Rise-time regimes a large in vibrated bulk solids, Phys. Rev. Lett. 78 (7) (1997) 1255–1258.
[22] E.R. Novak, J.B. Knight, M.L. Povinelli, H.M. Jaeger, S.R. Nagel, Reversibility and irreversibility in the packing of vibrated granular material, Powder Technol. 94 (1997) 79–83.
[23] N. Zhang, A.D. Rosato, Experiments and simulations on vibration induced densification of bulk solids, Kona J. 24 (2006) 93–103.
[24] P. Richard, P. Philippe, F. Barbe, S. Bourles, X. Thibault, D. Bideau, Analysis by x-ray microtomography of a granular packing undergoing compaction, Phys. Rev. E 68 (2003), 020301.
[25] T. Aste, M. Saadatfar, A. Sakellariou, T.J. Senden, Investigating the geometrical structure of disordered sphere packings, Phys. A 339 (2004) 16–23.
[26] T. Aste, M. Saadatfar, T.J., Geometrical structure of disordered sphere packings, Phys. Rev. E 71 (2005) 061302.
[27] K.E. Daniels, R.P. Behringer, Hysteresis and competition between disorder and crystallization in sheared and vibrated granular flow, Phys. Rev. Lett. 94 (2005) 168001.
[28] X.Z. An, C.X. Li, R.Y. Yang, R.P. Zou, A.B. Yu, Experimental study of the packing of mono-sized spheres subjected to one-dimensional vibration, Powder Technol. 196 (2009) 50–55.
[29] X.Z. An, C.X. Li, Experiments on densifying of equal spheres by two-dimensional vibration, Particuology 11 (2013) 689–694.
[30] C.X. Li, X.Z. An, R.Y. Yang, R.P. Zou, A.B. Yu, Experimental study on the packing of uniform spheres under three-dimensional vibration, Powder Technol. 208 (2011) 617–622.
[31] J.S. Goodling, R.I. Vachon, W.S. Stelpflug, S.J. Ying, M.S. Khader, Radial porosity distribution in cylindrical beds packed with spheres, Powder Technol. 35 (1983).
[32] A.J. Sederman, P. Alexander, L.F. Gladden, Structure of packed beds probed by magnetic resonance imaging, Powder Technol. 117 (2001) 255–269.
[33] G.E. Mueller, Angular void fraction distribution in randomly packed fixed beds of uniformly sized spheres in cylindrical containers, Powder Technol. 77 (1993) 313–319.
[34] W. van Antwerpen, C.G. du Toit, P.G. Rousseau, A review of correlations to model the packing structure and effective thermal conductivity in packed beds of mono-sized spherical particles, Nucl. Eng. Des. 240 (2010) 1803–1818.
[35] G.T. Seidler, G. Martinez, L.H. Seeley, K.H. Kim, E.A. Behne, S. Zaranek, B.D. Chapman, S.M. Heald, D.L. Brewe, Granule-by-granule reconstruction of a sandpile from x-ray microtomography data, Phys. Rev. E 62 (6) (2000) 8175–8181.
[36] F. Scaffidi-Argentina, G. Piazza, A. Goraieb, E. Boller, A. Elmoutaouakkil, C. Ferrero, J. Baruchel, Non-destructive three-dimensional analysis of the packing of a binary beryllium pebble bed, Fusion Eng. Des. 58–59 (2001) 707–712.
[37] J. Reimann, R.A. Pieritz, M. di Michiel, C. Ferrero, Inner structures of compressed pebble beds determined by X-ray tomography, Fusion Eng. Des. 75-79 (2005) 1049–1053.
[38] G.A. Georgalli, M.A. Reuter, Modelling the co-ordination number of a packed bed of spheres with distributed sizes using a CT scanner, Miner. Eng. 19 (2006) 246–255.
[39] J. Reimann, R.A. Pieritz, R. Rolli, Topology of compressed pebble beds, Fusion Eng. Des. 81 (2006) 653–658.
[40] X. Fu, M. Dutt, A. Bentham, B. Hancock, R.E. Cameron, J.A. Elliott, Investigation of particle packing in model pharmaceutical powders using x-ray microtomography and discrete element method, Powder Technol. 167 (2006) 134–140.
[41] J. Reimann, R.A. Pieritz, C. Ferrero, M. di Michiel, R. Rolli, Inner structures of compressed pebble beds determined by X-ray tomography, Fusion Eng. Des. 83 (2008) 1326–1330.
[42] M. Suzuki, T. Shinmura, K. Limura, M. Hirota, Study of the wall effect on particle packing structure using x-ray micro computed tomography, Adv. Powder Technol. 19 (2008) 183–195.
[43] R.A. Pieritz, J. Reimann, C. Ferrero, 3D tomography analysis of the inner structure of pebbles and pebble beds, Adv. Eng. Mater. 13 (2011) 145–155.
[44] C.M. Wensrich, Boundary structure in dense random pack monosize spherical particles, Powder Technol. 219 (2012) 118–127.
[45] J. Reimann, A. Abou-Sena, R. Nippen, P. Tafforeau, Pebble bed packing in square cavities, Fusion Eng. Des. 88 (2013) 2343–2347.
[46] P. Langston, A.R. Kennedy, Discrete element modelling of the packing of spheres and its application to the structure of porous metals made by infiltration of packed beds of NaCl beads, Powder Technol. 268 (2014) 210–218.
[47] J. Reimann, E. Brun, C. Ferrero, J. Vicente, Pebble bed structures in the vicinity of concave and convex walls, Fusion Eng. Des. 98-99 (2015) 1855–1858.
[48] Y. Wang, C.L. Lin, J.D. Miller, Improved 3D image segmentation for x-ray tomographic analysis of packed particle beds, Miner. Eng. 83 (2015) 185–191.
[49] P.A. Cundall, O.D.L. Strack, A discrete element model for granular assemblies, Geotechnique 29 (1979) 1055–1066.
[50] B.A. Klumov, Y. Jin, H.A. Makse, Structural properties of dense hard sphere packings, J. Phys. Chem. B (2014) (in press).
[51] P. Mort, et al., Dense granular flow – a collaborative study, Powder Technol. 284 (2015) 571–584.
[52] X. Gan, M. Kamlah, J. Reimann, Computer simulation of packing structure in pebble beds, Fusion Eng. Des. 85 (2010) 1782–1787.
[53] G.W. Delaney, T. Di Matteo, T. Aste, Combining tomographic imaging and DEM simulations to investigate the structure of experimental sphere packings, Soft Matter 6 (2010) 2992–3006.
[54] J. Reimann, L. Boccaccini, M. Enoeda, A. Ying, Thermomechanics of solid breeder and Be pebble bed materials, Fusion Eng. Des. 61-62 (2002) 319–331.
[55] C.G. du Toit, Radial variation in porosity in annular packed beds, Nucl. Eng. Des. 238 (2008) 3073–3079.
[56] A. Abou-Sena, H. Neuberger, T. Ihli, Experimental investigation on the possible techniques of pebbles packing for the HCPB Test Blanket Module, Fusion Eng. Des. 84 (2009) 355–358.
[57] J. Reimann, A. Abou-Sena, R. Nippen, C. Ferrero, Pebble bed packing in square cavities, KIT Scientific Reports 2012, p. 7631.
[58] N. Mueggenburg, Granular compaction under confinement, Phys. Rev. E 85 (2012) 041305.
[59] E.E. Ehrichs, H.M. Jaeger, G.S. Karczmar, J.B. Knight, V.Y. Kuperman, S.R. Nagel, Granular convection observed by magnetic resonance imaging, Science 267 (1995) 1632–1634.
[60] E. Clement, J. Duran, J. Rajchenbach, Experimental study of heaping in a two-dimensional "sandpile", Phys. Rev. Lett. 69 (8) (1992) 1189–1192.
[61] S.-C. Tai, S.-S. Hsiau, The flow regime during the crystallization state and convection state on a vibrating granular bed, Adv. Powder Technol. 20 (2009) 335–349.
[62] T.M. Yamada, H. Katsuragi, Scaling of convective velocity in a vertically vibrated granular bed, Planet. Space Sci. 100 (2014) 79–86.
[63] X. An, R. Yang, K. Dong, A. Yu, DEM study of crystallization of monosized spheres under mechanical vibration, Comput. Phys. Commun. 182 (2011) 1980–1994.
[64] T. Weitkamp, et al., Status and Evolution of ESRF Beamline ID 19, AIP Conf. Proc. (ICXOM20), vol 1221, 2010, pp. 33–38.
[65] S. Sanchez, V. Fernandez, S.E. Pierce, P. Tafforeau, Homogenization of sample absorption for the imaging of large and dense fossils with synchrotron microtomography, Nat. Protoc. 8 (2013) (1708) 1717.
[66] A. Koch, Lens coupled scintillating screen-CCD X-ray area detector with a high quantum efficiency, Nucl. Inst. Methods Phys. Res. A (1994) 654–658.
[67] J.-C. Labiche, et al., The fast readout low noise camera as a versatile x-ray detector for time resolved dispersive extended x-ray absorption fine structure and diffraction studies of dynamic problems in materials science, chemistry, and catalysis, Rev. Sci. Instrum. 78 (2007) 0901301.
[68] J. Vicente, F. Topin, J.V. Daurelle, Open celled material structural properties measurement: from morphology to transport properties, Mater. Trans. 47 (9) (2006) 2195–2202.
[69] S. Beucher, Image Vis. Comput. 25 (4) (2007) 405–415.
[70] J. Vicente, Y. Wyart, P. Moulin, Characterization (two dimensional-three-dimensional) of ceramic microfiltration membrane by synchrotron radiation: new and abraded membranes, J. Porous Media 01 (16) (2013) 537–545.